

Coherent diffractive imaging of single helium nanodroplets with a high harmonic generation source

Daniela Rupp¹, Nils Monserud², Bruno Langbehn¹, Mario Sauppe¹, Julian Zimmermann¹, Yevheniy Ovcharenko¹, Thomas Möller¹, Fabio Frassetto³, Luca Poletto³, Andrea Trabattoni⁴, Francesca Calegari⁵, Mauro Nisoli^{4,5}, Katharina Sander⁶, Christian Peltz⁶, Marc J. J. Vrakking², Thomas Fennel⁶ & Arnaud Rouzée²

¹*Institut für Optik und Atomare Physik, Technische Universität Berlin, Hardenbergstraße 36, 10623 Berlin, Germany*

²*Max-Born-Institut für Nichtlineare Optik und Kurzzeitspektroskopie, Max-Born-Straße 2A, 12489 Berlin, Germany*

³*CNR, Istituto di Fotonica e Nanotecnologie Padova, Via Trasea 7, 35131 Padova, Italy*

⁴*Department of Physics, Politecnico di Milano, Piazza L. da Vinci 32, 20133 Milano, Italy*

⁵*CNR, Istituto di Fotonica e Nanotecnologie Milano, Piazza L. da Vinci 32, 20133 Milano, Italy*

⁶*Institut für Physik, Universität Rostock, Albert-Einstein-Straße 23, 18059 Rostock, Germany*

Coherent diffractive imaging of individual free nanoparticles has opened novel routes for the in-situ analysis of their transient structural, optical, and electronic properties. So far, single-particle diffraction was assumed to be feasible only at extreme ultraviolet (XUV) and X-ray free-electron lasers, restricting this research field to large-scale facilities. Here we demonstrate single-shot imaging of isolated helium nanodroplets using XUV pulses from a femtosecond-laser driven high harmonic source. We obtain bright scattering patterns that

provide access to the nanostructure’s optical parameters. Moreover, the wide-angle scattering data enable us to uniquely identify hitherto unresolved prolate shapes of superfluid helium droplets. Our results mark the advent of single-shot gas-phase nanoscopy with lab-based short-wavelength pulses and pave the way to ultrafast coherent diffractive imaging with phase-controlled multicolor fields and attosecond pulses.

Single-shot coherent diffractive imaging (CDI) with intense short-wavelength pulses became possible just recently with the advent of XUV and X-ray free-electron lasers (FEL) ¹. This lensless imaging method has revolutionized the structural characterization of nanoscale samples including biological specimens ², aerosols ³, and atomic clusters ⁴⁻⁶. By capturing high quality diffraction patterns from a single nanoparticle in free flight using a single laser pulse, the sample morphology in-situ and free from spurious interactions due to deposition on a substrate can be determined. When exploiting the tomographic information contained in wide-angle scattering, a single diffraction image can even reveal the full three-dimensional particle shape and orientation ⁶⁻⁸. This unique capabilities enable the investigation of metastable or transient states that exist only in the gas phase. Pioneering FEL experiments have explored this frontier and demonstrated CDI of quantum vortices in helium droplets ⁵, ultrafast nanoplasma formation ⁹, and explosion of laser-heated clusters ¹⁰. The ability to perform single-shot nanoparticle CDI using XUV and soft X-ray high harmonic generation (HHG) sources would allow to combine the nanoscale structural imaging capabilities of CDI with the exquisite temporal, spectral, and phase control inherent in the use of optical lasers, including the fascinating prospect of CDI with isolated attosecond pulses.

HHG sources typically have a brightness that is orders of magnitude lower than that of an FEL¹¹, but over the years a number of them have been scaled up in order to achieve high intensities and/or high average power^{12–17}, allowing coherent diffractive imaging of fixed targets^{18–23}. Experiments on ion-beam edged nanostructures in membranes achieved impressive resolution on the order of 20 nm after multiple exposures^{22,23} and even yielded the overall shape from a single-shot diffraction image in favorable cases²⁰. Here we report the feasibility of lab-based 3D characterization of unsupported nanoparticles and demonstrate single-shot HHG-CDI on individual free helium nanodroplets.

In our experiment (Fig. 1), a high power Ti:sapphire laser amplifier was used to generate 35 fs laser pulses at 792 nm wavelength with up to 33 mJ pulse energy. About 12 mJ were loosely focused ($f = 5$ m) into a xenon-filled gas cell²⁴, producing approximately 2 μ J of XUV radiation. The CDI application requires high flux and thus tight focusing. Typical back-reflection multilayer mirrors, however, conflict with the use of straylight apertures and the detection of scattered light at small scattering angles. Therefore, CDI-compatible grazing-incidence microfocusing optics with an overall transmission of 10% based on a coma-correcting system of toroidal mirrors²⁵ were used to focus the multicolor XUV beam to a small spot (beam-waist $\omega_0 = 10\mu\text{m}$), achieving a power density of 3×10^{12} W/cm² (pulse averaged). The XUV spectrum (11th to 17th harmonic, see Fig. 2e) was obtained prior to the CDI measurements with a grating spectrometer. A jet of helium droplets with diameters of several hundreds of nanometers crossed the focus of the XUV beam. The droplets were generated using a cryogenically cooled pulsed valve maintained at a temperature between 4.9 K and 5.7 K, operating at low repetition rates of 3-10 Hz. The diffracted radiation was

measured shot-to-shot with a wide-area MCP-based (micro-channel plate) scattering detector (see methods).

A dataset of 2300 single-shot diffraction patterns of single helium droplets with distinct structures was obtained. The large majority of diffraction patterns ($\approx 76\%$) shows ring structures that can be assigned to spherical droplets (see examples in Fig. 2a and c). For these simple structures, the scattering images give access to the optical properties of the droplets when exploiting the multi-color nature of the XUV pulses. The diffracted field from dielectric spheres illuminated with a single wavelength can be described by the Mie solution and yields scattering patterns showing concentric rings. The ring separation scales with the wavelength and with the inverse particle size. The overall scattering strength and the detailed shape of the ring structure further depend on the material's complex refractive index. In our case, the XUV pulses contain spectral contributions from four harmonics (Fig. 2e). Therefore the scattering pattern is a superposition of the corresponding single-wavelength scattering intensities, and displays a characteristic beating pattern due to the wavelength-dependent ring spacings of the individual spectral contributions to the image (see Fig. 2b and 2d). For a known XUV spectrum, the remaining parameters in the multicolor fit of the scattering pattern are the spherical particle's size and its refractive indices at the wavelengths of the contributing harmonics. Hence, the optical properties of an individual nanoparticle can be characterized in-situ on a single-shot basis.

The optical parameters of bulk liquid helium and helium nanodroplets are not well known in the photon energy range considered here ^{26,27} and may substantially change with droplet size ²⁸.

In fact, the calculated multicolor Mie scattering patterns do not match the measurements when using the bulk literature values for the refractive indices at the corresponding harmonic wavelengths (see supplemental figure). In order to fit the observed patterns, we employed a multidimensional optimization (see methods) to determine both the particle size and the refractive indices at the wavelengths of the dominant 13th and 15th harmonics. The refractive indices at the wavelengths of the 11th and 17th harmonics were fixed, as they lie far away from the large helium resonances²⁷. The relative intensities of the contributing harmonics were extracted from the average spectrum in Fig. 2e. Eight very bright scattering patterns with clear beating structures up to maximum scattering angles were analysed. As exemplified in Fig. 2b and 2d, good matches between experimental and calculated profiles can be found with optimized optical parameters, that deviate substantially from the bulk values (cf. Fig. 2f). However, the scatter of the fitting results remains large, which is mainly attributed to shot-to-shot fluctuations in the XUV spectrum and poor signal-to-noise ratio at large scattering angles. These experimental deficiencies have to be overcome to enable probing the size-dependent refractive indices of nanoparticles via single shot CDI in future systematic studies. For example, using higher energy and/or lower wavelength drivers, it is anticipated that the photon flux of individual harmonics can be further increased by at least one order of magnitude¹⁷.

Besides concentric ring patterns and an abundance of about 20% of elliptical patterns from ellipsoidal droplets, about 3% of all bright images exhibit pronounced streak structures as exemplified in Fig. 3a. The abundance of these three main types of patterns is similar to what has been reported in previous hard X-ray measurements at LCLS⁵. However, whereas straight streak patterns were observed in the X-ray results, we find in the majority of our wide-angle scattering

patterns a pronounced crescent-shaped bending of the streaks (cf. Fig. 3a, 3b). In the X-ray experiments, the reconstruction of the corresponding droplet shapes via iterative phase retrieval revealed 2D projections of the helium droplets with extreme aspect ratios⁵. These were attributed to classically unstable oblate droplets with a wheel-like shape rotating with a high angular momentum, that can only exist in the superfluid phase⁵. Very recently these results were further supported by statistical arguments, while an indication of rare prolate structures was also found²⁹. However, a unique discrimination of prolate and oblate shapes based on the 2D projections accessible with small-angle X-ray diffraction is difficult²⁹. Tomographic information, on the other hand, is contained in XUV wide-angle scattering⁸ and can be exploited to retrieve the three-dimensional particle shape and orientation provided the particle morphology is sufficiently regular^{6,7}. In our measurement, the presence of tomographic information manifests in the considerable bending of the streak patterns.

In order to retrieve the shapes underlying the experimentally observed scattering patterns, three dimensional multi-color scattering simulations were performed³⁰ (see methods). The two-sided, bent streak features can only be reproduced considering prolate droplets with a pill shape as shown in Fig. 3c, matching the experimental pattern of Fig. 3b. Crescent-shaped streaks arise from prolate structures that are tilted out of the scattering plane (i.e. the plane normal to the laser propagation axis). In contrast, as exemplified in Fig. 3d, a tilted wheel-shaped particle with the same aspect ratio cannot explain the bending of the streaks. Instead, in the wide-angle scattering regime, the simulations indicate that such particles would generate a one-sided straight streak, a phenomenon that was not observed in our experiment. We would like to note that the absence of

wheel-shaped droplets in our experiment may stem from the different droplet generation scheme, using a pulsed valve with a long nozzle in this work, where the transition to the superfluid state might be delayed compared to the short cw flow nozzle used by Gomez et al.⁵ However, our results unambiguously determine the strongly deformed helium droplets in our experiment to be pill-shaped, benefitting from the three-dimensional tomographic nature of scattering in the XUV regime. The observation of pill-shaped droplets, which would also be expected for classical liquids³¹, will contribute to the discussion on the stability of spinning superfluid droplets.

We have shown the feasibility of single-shot single particle coherent diffractive imaging using intense XUV pulses from a high harmonic generation source. Bright diffraction patterns of spherical helium droplets have been obtained and matched with simulations using optimized refractive indices, whereas characteristic crescent-shaped streak patterns could be uniquely assigned to pill-shaped droplets. Further, the experiment suggests a number of very exciting future prospects. Laser-based HHG facilities provide a high accessibility compared to free-electron lasers in a wavelength regime suitable for 3D shape characterization of non-reproducible gas-phase nanoobjects. This will facilitate fundamental investigations of structure formation, such as tracing ice nucleation³², with important implications for atmospheric physics and aerosol science. Moreover, highly interesting experiments beyond structural determination are possible, such as multicolor tomography and resonant-pump - resonant-probe CDI, that exploit the time-resolution and phase control achievable in HHG-based experiments for diffractive imaging of quantum coherent dynamics. Probably the most exciting prospect of HHG-CDI will be to make use of the attosecond capabilities of HHG sources for time resolved imaging - a vision that has been driving

attosecond science from its beginning^{33,34}.

Methods

Femtosecond laser system and generation of XUV harmonics. The experiments are performed using a commercially available cryo-cooled Ti:sapphire laser amplifier (KMLabs Red Wyvern) delivering pulses at a central wavelength of 792 nm with 33 mJ pulse energy and 35 fs pulse duration at a 1 kHz repetition rate. 30% of the output energy (typically 10-12 mJ) are taken for the generation of high harmonics. To this aim, a broadband spherical mirror with a focal distance of 5 m is used to focus the near-infrared pulses into a 100 mm long aluminum gas cell statically filled with ≈ 1.3 mbar of xenon (loose focusing geometry). The position of the gas cell, the gas pressure and the NIR pulse energy are adjusted to optimize the HHG flux. An output energy of approximately 2 μ J (measured with a calibrated photodiode) is achieved in this geometry, corresponding to a conversion efficiency of 1.6×10^{-4} and an average power of 2 mW. To the best of our knowledge, this is the highest average power obtained by means of HHG. The harmonic beam consists of the 11th (72 nm), 13th (61 nm), 15th (53 nm), and 17th (47 nm) harmonics (see Fig. 2e) as measured by dispersing the XUV beam with a grating spectrometer. The XUV pulse duration was characterized in previous experiments using THz electron streaking technique to be roughly 20 fs.

Microfocusing setup and IR filter. A high throughput XUV beamline (transmission $\approx 10\%$) consisting of three gold-coated, grazing incidence (10°) toroidal mirrors and a flat Mo/Si mirror is used to tightly focus the XUV beam onto the target sample. Positions, radii and distances between the toroidal mirrors were optimized by ray tracing in order to achieve a high demagnification

factor of 25 for the XUV beam while keeping the coma-aberrations low^{25,35}. The first 40 mm \times 10 mm toroidal mirror with radii 57.6 m \times 1.735 m is placed 5 m away from the gas cell in order to collimate the XUV beam. The collimated beam is then reflected by a flat Mo/Si mirror that partially absorbs the co-propagating near-infrared (NIR) laser pulse used for HHG. The remaining NIR laser beam (\approx 1 mJ) is filtered out by a 100 nm thin aluminium filter. We note that the reduction of the NIR by the Mo/Si mirror is required to avoid damaging the aluminium foil. A coma-corrected system composed of two toroidal mirrors facing each other is then used to demagnify and tightly focus the XUV beam into the experimental chamber. The first of the latter two toroidal mirrors (radii 2650 mm \times 79 mm) focuses the XUV beam approximatively 230 mm away from the mirror whereas the last toroidal mirror (radii 3620 mm \times 109.2 mm) is placed 680 mm away from the focus and is used to relay image the focus of the first toroidal mirror into the experimental chamber at a distance of 585 mm. This geometry allows a demagnification factor of 25 with respect to the initial XUV spot size at the generation point. Considering a 0.5 mrad \times 0.5 mrad diverging XUV beam with a 175 μ m spotsize (FWHM) at the source point, we expect to achieve a minimum spot size at the focus of 7 μ m (FWHM). In our experiment, the size of the XUV beam was characterized by monitoring the fluorescence of a Cs/YAG screen placed at the focus using a CCD camera. We measured a 9 μ m \times 10 μ m spot size (FWHM) with a 10 μ m beam waist, in close agreement with the expected value leading to an intensity of $I_f = 3 \times 10^{12}$ W/cm².

Helium droplet generation. The helium nanodroplets are generated with a pulsed Even-Lavie valve³⁶ that is cooled with a Sumitomo closed-cycle cryostat down to 4.9 K - 5.7 K. The minimum temperature depends on the repetition rate and the opening duration of the valve (varied between

3 and 10 Hz and 18 to 27 μ s, respectively) which influence the heat load of the valve. High-purity helium (99.9999%) at a pressure of 80 bars is expanded into a differentially pumped UHV chamber through a 100 μ m trumpet shaped nozzle located at 450 mm distance to the interaction region. The droplet pulse is guided into the interaction chamber through a conical skimmer with 1 mm diameter, which reduces the uncondensed gas in the interaction chamber.

Scattering experiment. A large-area scattering detector (\varnothing 75 mm) with a center hole (\varnothing 3 mm) diameter is placed 37 mm behind the XUV focus, corresponding to a maximum spatial frequency of 0.09 nm⁻¹ for the dominant wavelength of 53 nm. The detector consists of a Chevron-type MCP for signal amplification and a phosphor screen for conversion to optical light⁴. The MCP is used in pulsed operation to suppress background signal from charged particles. Further, the CDI-compatible focusing geometry described above allows for the use of two straylight apertures before the focus to minimize photonic background signal on the detector. The 8° tilt of the MCP channels results in an area with decreased response observable at the lower right side of the detector hole (cf. Fig. 2, Fig. 3)³⁷. The scattering patterns are recorded on a shot-to-shot basis using an out-of-vacuum CMOS camera. An ion time-of-flight spectrometer is used for establishing and optimizing the spatial overlap of the XUV pulses and the helium nanodroplets and the timing of the droplet jet³⁸. Within 3×10^5 single-shot measurements 2300 bright patterns with distinct structures were obtained and another 12700 recorded images contained weak, unstructured scattering signal. The statistics indicate that the experiment is performed in the single-particle limit, i.e. the probability to have two droplets in the focus at the same time is low.

Scattering simulations. For comparison with theory, the measured diffraction patterns are transformed to the scattered intensity that would be recorded on a spherical detector and corrected for the nonlinear detector response⁶. The detected intensity I_{det} is assumed to scale exponentially with the true experimental intensity I_{exp} , via $I_{\text{det}} = I_{\text{exp}}^{\text{alpha}}$. A nonlinearity exponent $\text{alpha}=0.5$ is used, for which the angular decay of the scattering profiles matches Porod’s law³⁹. In order to fit the measured patterns for spherical particles, we employ a multidimensional Simplex optimization⁴⁰ on the basis of multi-color Mie scattering calculations^{41,42}. The intensity pattern in a calculated multi-color image contains four single-frequency-components (11th to 17th harmonic), each weighted with the intensity of the respective harmonic order. The remaining parameters are the particle size and the photon energy-dependent refractive indices. For helium, the 11th and 17th harmonics are far away from resonances^{26,27}, so that literature values of the refractive indices can be fixed within the fit procedure (17.2 eV: $n = 0.97 + i0.0$; 26.6 eV: $n = 0.9964 + i0.041$)⁴³. This results in a total of five remaining optimization parameters, i.e. the droplet radius and the real and imaginary part of the complex refractive indices of the 13th and 15th harmonic. Eight measured patterns with clear rings up to maximum scattering angle were fitted using a hybrid Monte-Carlo Simplex optimization algorithm for a large ensemble of trajectories (see supplemental figure). Each fitting trajectory was initialized with random start parameters in a reasonable range for the corresponding optimization parameters ($R = 300 \text{ nm}$ to $R = 600 \text{ nm}$, $\delta = -0.3$ to $\delta = 0.2$, $\beta = 0$ to $\beta = 0.07$), and subsequently improved via Simplex optimization. The scattering patterns for nonspherical shapes are calculated in the discrete-dipole-approximation as implemented in Ref.³⁰ by the superposition of four single-color calculations and using the average optical parameters of

the 13th and 15th harmonic determined in our study (20.4 eV: $n = 0.9302 + i0.0165$; 23.5 eV: $n = 1.2561 + i0.0337$).

1. Chapman, H. & Nugent, K. Coherent lensless X-ray imaging. *Nat. Phot.* **4**, 833–839 (2010).
2. Seibert, M. *et al.* Single mimivirus particles intercepted and imaged with an X-ray laser. *Nature* **470**, 78–81 (2011).
3. Loh, N. *et al.* Fractal morphology, imaging and mass spectrometry of single aerosol particles in flight. *Nature* 513–517 (2012).
4. Bostedt, C. *et al.* Clusters in intense FLASH pulses: ultrafast ionization dynamics and electron emission studied with spectroscopic and scattering techniques. *J. Phys. B* **43**, 194011 (2010).
5. Gomez, L. *et al.* Shapes and vorticities of superfluid helium nanodroplets. *Science* **345**, 906–909 (2014).
6. Barke, I. *et al.* The 3D-architecture of individual free silver nanoparticles captured by X-ray scattering. *Nat. Comm.* **6**, 6187 (2015).
7. Xu, R. *et al.* Single-shot three-dimensional structure determination of nanocrystals with femtosecond X-ray free-electron laser pulses. *Nat. Comm.* **5**, 4061 (2014).
8. Raines, K. *et al.* Three-dimensional structure determination from a single view. *Nature* **463**, 7278 (2009).

9. Bostedt, C. *et al.* Ultrafast x-ray scattering of xenon nanoparticles: Imaging transient states of matter. *Phys. Rev. Lett.* **108**, 093401 (2012).
10. Gorkhover, T. *et al.* Femtosecond and nanometre visualization of structural dynamics in superheated nanoparticles. *Nat. Phot.* **10**, 93 (2016).
11. Miao, J., Ishikawa, T., Robinson, I. K. & Murnane, M. M. Beyond crystallography: Diffractive imaging using coherent x-ray light sources. *Science* **348**, 530–535 (2015).
12. Hergott, J.-F. *et al.* Extreme-ultraviolet high-order harmonic pulses in the microjoule range. *Phys. Rev. A* **66**, 021801 (2002).
13. Hädrich, S. *et al.* Generation of μW level plateau harmonics at high repetition rate. *Opt. Express* **19**, 19374–19383 (2011).
14. Rudawski, P. *et al.* A high-flux high-order harmonic source. *Rev. Sci. Instr.* **84** (2013).
15. Takahashi, E. J., Lan, P., Mücke, O., Nabekawa, Y. & Midorikawa, K. Attosecond nonlinear optics using gigawatt-scale isolated attosecond pulses. *Nat. Comm.* **4** (2013).
16. Hong, K.-H. *et al.* Multi-mJ, kHz, $2.1\ \mu\text{m}$ optical parametric chirped-pulse amplifier and high-flux soft x-ray high-harmonic generation. *Opt. Lett.* **39**, 3145–3148 (2014).
17. Popmintchev, D. *et al.* Ultraviolet surprise: Efficient soft x-ray high-harmonic generation in multiply ionized plasmas. *Science* **350**, 1225–1231 (2015).

18. Miao, J., Ishikawa, T., Anderson, E. H. & Hodgson, K. O. Phase retrieval of diffraction patterns from noncrystalline samples using the oversampling method. *Phys. Rev. B* **67**, 174104 (2003).
19. Sandberg, R. L. *et al.* Lensless diffractive imaging using tabletop coherent high-harmonic soft-x-ray beams. *Phys. Rev. Lett.* **99**, 098103 (2007).
20. Ravasio, A. *et al.* Single-shot diffractive imaging with a table-top femtosecond soft x-ray laser-harmonics source. *Phys. Rev. Lett.* **103**, 028104 (2009).
21. Chen, B. *et al.* Multiple wavelength diffractive imaging. *Phys. Rev. A* **79**, 023809 (2009).
22. Seaberg, M. D. *et al.* Ultrahigh 22 nm resolution coherent diffractive imaging using a desktop 13 nm high harmonic source. *Opt. Express* **19**, 22470–22479 (2011).
23. Zürich, M. *et al.* Real-time and Sub-wavelength Ultrafast Coherent Diffraction Imaging in the Extreme Ultraviolet. *Scientific Reports* **4**, 7356 (2014).
24. Schütte, B., Arbeiter, M., Fennel, T., Vrakking, M. J. J. & Rouzée, A. Rare-gas clusters in intense extreme-ultraviolet pulses from a high-order harmonic source. *Phys. Rev. Lett.* **112**, 073003 (2014).
25. Frassetto, F. *et al.* High-throughput beamline for attosecond pulses based on toroidal mirrors with microfocusing capabilities. *Rev. Sci. Instr.* **85** (2014).
26. Surko, C. M., Dick, G. J., Reif, F. & Walker, W. C. Spectroscopic study of liquid helium in the vacuum ultraviolet. *Phys. Rev. Lett.* **23**, 842–846 (1969).

27. Lucas, A. A., Vigneron, J. P., Donnelly, S. E. & Rife, J. C. Theoretical interpretation of the vacuum ultraviolet reflectance of liquid helium and of the absorption spectra of helium microbubbles in aluminum. *Phys. Rev. B* **28**, 2485–2496 (1983).
28. Joppien, M., Karnbach, R. & Möller, T. Electronic excitations in liquid helium: The evolution from small clusters to large droplets. *Phys. Rev. Lett.* **71**, 2654–2657 (1993).
29. Bernando, C. *et al.* Shapes of rotating superfluid helium nano-droplets. *in preparation* (2016).
30. Sander, K. *et al.* Influence of wavelength and pulse duration on single-shot x-ray diffraction patterns from nonspherical nanoparticles. *Journal of Physics B: Atomic, Molecular and Optical Physics* **48**, 204004 (2015).
31. Brown, R. A. & Scriven, L. E. The shape and stability of rotating liquid drops. *Proceedings of the Royal Society of London A: Mathematical, Physical and Engineering Sciences* **371**, 331–357 (1980).
32. Levin, Z. & Cotton, W. Recommendations. In Levin, Z. & W.R., C. (eds.) *Aerosol Pollution Impact on Precipitation* (Springer, Netherlands, 2009).
33. Niikura, H. & Corkum, P. Attosecond and angstrom science. *Advances In Atomic, Molecular, and Optical Physics* **54**, 511 – 548 (2007).
34. Krausz, F. & Ivanov, M. Attosecond physics. *Rev. Mod. Phys.* **81**, 163–234 (2009).
35. Poletto, L. *et al.* Micro-focusing of attosecond pulses by grazing-incidence toroidal mirrors. *Opt. Express* **21**, 13040–13051 (2013).

36. Even, U. The even-lavie valve as a source for high intensity supersonic beam. *EPJ Techniques and Instrumentation* **2**, 1–22 (2015).
37. Fukuzawa, H. *et al.* Electron spectroscopy of rare-gas clusters irradiated by x-ray free-electron laser pulses from sacra. *J. Phys. B* **49**, 034004 (2016).
38. Rupp, D. *et al.* Generation and structure of extremely large clusters in pulsed jets. *J. Chem. Phys.* **141**, 044306 (2014).
39. Sorensen, C. & Fischbach, D. Patterns in mie scattering. *Optics Communications* **173**, 145 – 153 (2000).
40. Lagarias, J. C., Reeds, J. A., Wright, M. H. & Wright, P. E. Convergence properties of the nelder–mead simplex method in low dimensions. *SIAM Journal on Optimization* **9**, 112–147 (1998).
41. Mie, G. Beiträge zur Optik trüber Medien, speziell kolloidaler Metallösungen. *Annalen der Physik* (1908).
42. Bohren, C. & Huffman, D. *Absorption and scattering of light by small particles* (John Wiley, 1983).
43. <http://physics.nist.gov/PhysRefData/FFast/html/form.htm>. NIST on-line data base.

Acknowledgements The authors kindly acknowledge Bernd Schütte’s excellent work for the initial development of the HHG beamline. The first author thanks Andrey Vilesov, Christoph Bostedt and Joachim

Ullrich for helpful and enlightening discussions. Excellent support has been provided by the TUB-IOAP workshop. This project has received funding from DFG (Grants No. BO 3169/2-2 and MO 719/13-1), from BMBF (Grant No. 05K13KT2), and from the European Union's Horizon 2020 research and innovation programme under the Marie Skłodowska-Curie grant agreement No 641789. Further, T.F. acknowledges computational resources provided by the North-German Supercomputing Alliance (HLRN) and financial support from the Deutsche Forschungsgemeinschaft via SFB652/3 and from BMBF (grant ID: 05K16HRB). F.C. and M.N. acknowledge funding from ERC grants STARLIGHT (637756), and ELYCHE (227355).

Competing Interests The authors declare that they have no competing financial interests.

Author Contributions D.R. and Y.O. did feasibility studies in advance of the experiment. F.F., L.P., A.T., F.C. and M.N. developed the microfocusing optics setup and implemented it together with N.M. and A.R. B.L. set up the helium jet, D.R. and M.S. set up the CDI detector, and J.Z. developed the data acquisition system. N.M. and A.R. run the HHG source, and D.R., M.S., B.L., N.M. and A.R. set up and carried out the experiment. D.R., N.M., B.L., J.Z., K.S., C.P., and T.F. analysed the data with input from all authors. The manuscript was discussed and written with input from all authors.

Correspondence Correspondence and requests for materials should be addressed to D.R., T.F., and A.R. (email: daniela.rupp@physik.tu-berlin.de, thomas.fennel@uni-rostock.de, arnaud.rouzee@mbi-berlin.de).

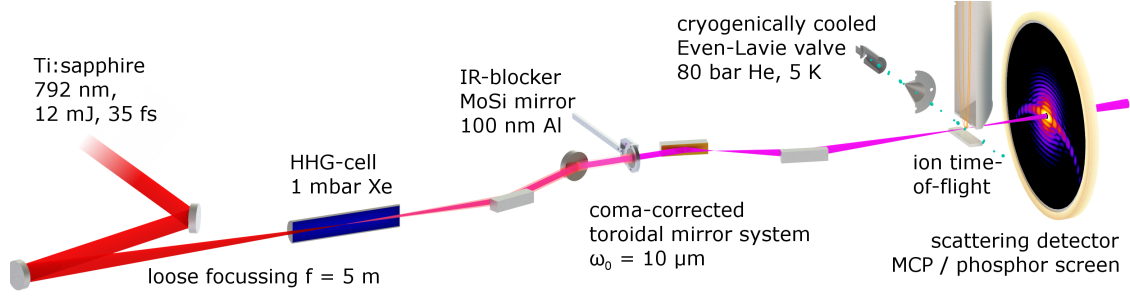


Figure 1: Scheme of the experimental setup. A Ti:sapphire laser with 792 nm central wavelength and 35 fs pulse duration is used for the generation of high harmonics. Up to 12 mJ are loosely focused into a xenon-filled cell, where the XUV pulses are produced. After removing the co-propagating NIR with a Mo/Si mirror and an aluminum filter, the beam is focused to a small spot ($\omega_0 = 10 \mu\text{m}$) using a coma-correcting system of gold-coated toroidal mirrors²⁵. A pulsed jet of helium nanodroplets ($\bar{R} \approx 500 \text{ nm}$) is overlapped with the XUV focus. The overlap is optimized by monitoring the formation of He^+ ions using an ion time-of-flight spectrometer. The scattering signal is amplified by a pulsed MCP and converted to optical photons on a phosphor screen. The single-shot diffraction images are captured with an out-of-vacuum camera.

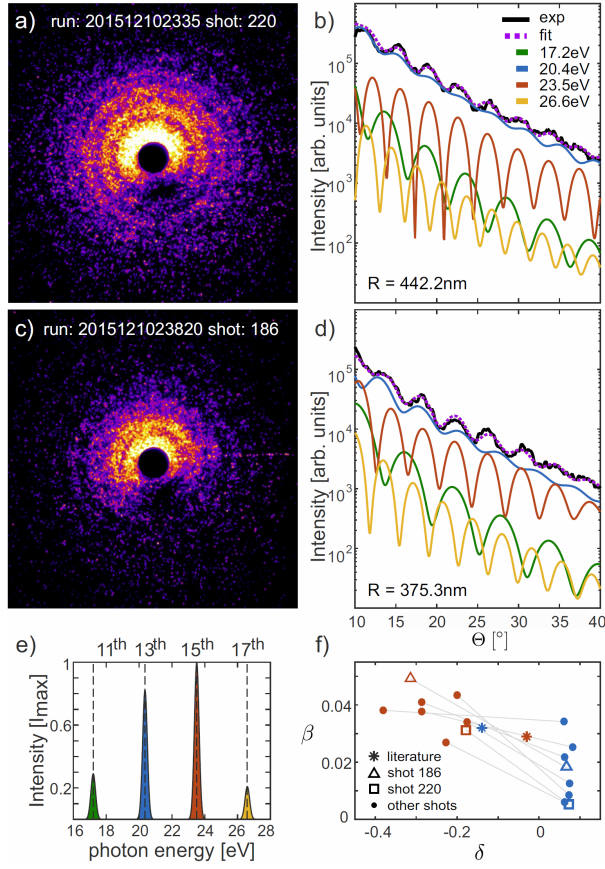


Figure 2: a) and c) Bright scattering patterns of spherical droplets showing pronounced concentric rings. b) and d) Corresponding radial intensity profiles (solid black). Multicolor Mie fits (dashed purple) are obtained via a simplex algorithm as described in the methods section. The harmonic contributions are given in green, blue, orange, and yellow. e) Measured average XUV spectrum of the HHG radiation. f) Optimized complex refractive indices $n = 1 - \delta - i\beta$ of the 13th and 15th harmonics obtained in the simplex-Mie fits for a selection of very bright scattering patterns with rings up to large scattering angles. Due to the absence of nearby resonances, the refractive index for the 11th and 17th harmonics are fixed at the literature values (see methods). The fitting values of β and δ for the 13th and 15th harmonics deviate considerably from the literature values.

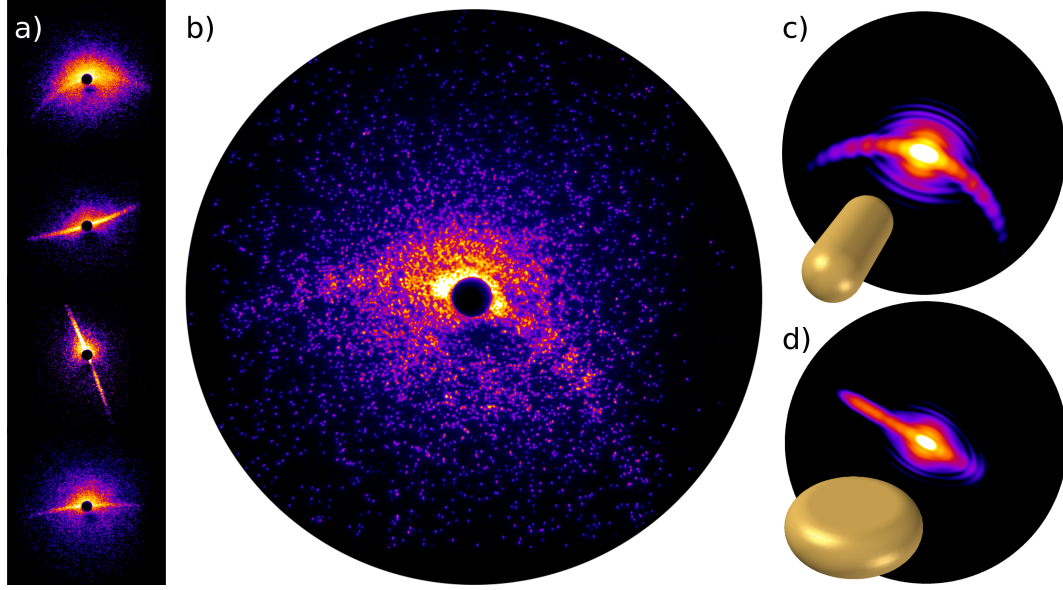


Figure 3: a) Examples for straight and bent streak patterns from single droplets that strongly deviate from spherical shape. b) Measured and c) matching simulated wide-angle diffraction image and visualization of a pill-shaped prolate droplet with short half-axis $a = b = 370$ nm and long half-axis $c = 950$ nm, tilted by 35° in respect to the laser propagation axis (further parameters see methods). d) Visualization and simulated wide-angle diffraction image of a wheel-shaped oblate particle. For angles between the symmetry axis of the particle and the laser propagation axis slightly different from 90° (here 80°), a straight streak to only one side is visible (long and short half-axes as in c), further parameters see methods).